

Synthesis of N-doped ZnO/ZnCo₂O₄ composites for stable photocatalytic degradation of organic dyes

Lukai Liu^{a,b}, Guoqing Zhao^{a,b,c}, Caifeng Li^{a,c}, Shu Zhou^a, Yinke Wang^a, Feipeng Jiao^{a,b,c,*}

^aSchool of Chemistry and Chemical Engineering, Central South University, Changsha 410083, China, Tel. +86 731 88830833; Fax: +86 731 88830833; emails: jiaofp@csu.edu.cn (F. Jiao), 315991663@qq.com (L. Liu), guoqingzhao@csu.edu.cn (G. Zhao), 1872860769@qq.com (C. Li), 2414657572@qq.com (S. Zhou), 1160489359@qq.com (Y. Wang)

^bHunan Provincial Key Laboratory of Efficient and Clean Utilization of Manganese Resources, Central South University, Changsha 410083, China

^cKey Laboratory of Hunan Province for Water Environment and Agriculture Product Safety, Changsha 410083, China

Received 27 March 2020; Accepted 1 December 2020

ABSTRACT

Based on the ZnCo-layered double hydroxides, the N-doped ZnO/ZnCo₂O₄ composites were successfully prepared via hydrothermal method. The as-synthesized composites were characterized by X-ray diffraction, scanning electron microscopy, high-resolution transmission electron microscopy, Fourier-transform infrared spectroscopy, N₂ adsorption–desorption analysis and UV-vis diffuse reflectance spectroscopy. The results showed that N-ZnO/ZnCo₂O₄ composites can support abundant oxygen vacancies to build ohmic contact and broaden the wavelength range of light absorption. Moreover, the methylene blue (MB), methyl orange (MO) and rhodamine B (RhB) were selected as the probe molecules to explore the photocatalytic performance of the N-ZnO/ZnCo₂O₄ composites. It was discovered that the removal efficiencies of MB, MO and RhB were approximately 91.66%, 90.95% and 91.22% within 210 min under visible light irradiation, respectively. The N-ZnO/ZnCo₂O₄ composites still maintain remarkable reusability and stability for degradation of the above three dyes after five successive cycles. Furthermore, the possible degradation mechanism of the N-ZnO/ZnCo₂O₄ composites was discussed in this work.

Keywords: N-doped ZnO/ZnCo₂O₄; Photodegradation; Oxygen vacancies; Organic dyes

1. Introduction

In recent decades, because of the high accessibility and low cost, synthetic dyes have been widely applied in paper production, food technology, textile printing and dyeing [1]. After entering into the water body without any pretreatments, the dye wastewater has been causing great danger to aquatic organisms and the ecological environment due to its high toxicity and complicated organic composition [2]. Therefore, developing an effective and rapid way to handle organic dyes has attracted extensive interest from environmental experts. In view of the above

hazards, various approaches have been widely exploited, including photocatalytic degradation, filtration, adsorption and biodegradation, etc [3]. Photocatalysis technology is the preferred alternative due to its high efficient decomposition, no secondary pollution, and lower energy consumption [4,5]. Therefore, it has great application potential in the environmental purification field.

As a kind of advanced oxidation technology, photocatalysis utilizing green solar energy has attracted significant attention. To this day, a large number of semiconductor materials have been rapidly developed, especially photocatalytic materials which play an important role in

* Corresponding author.

environmental purification [6,7]. Among many photocatalytic materials, ZnO has the unique advantages of low price, nontoxicity, and high photocatalytic activity [8,9]. However, its practical applications are limited because of some disadvantages such as poorly visible light absorbance, low charge separation efficiency and susceptibility to photo-corrosion [10,11]. Thus, modifying the surface and designing the internal structure of photocatalytic materials have been mentioned to overcome these defects and improve the photocatalytic efficiency [12–14].

At present, the regulation of oxygen vacancies (OVs) is an effective approach to surface modification technology. The defect levels between the valence band and conduction band are generated by the introduction of OVs, inducing new channels for light absorption [15–18]. Meanwhile, the photocatalytic performance is further enhanced by the influence of light absorption, charge transportation and separation, and surface reaction [19,20]. Aschauer et al. reported that the surface oxygen vacancies of TiO₂ can provide some sites for direct adsorption and activation of O₂, contributing to the production of reactive oxygen species [21,22]. Some studies showed that the local state induced by OVs can expand the photoreaction range and effectively capture electrons, enhancing the photoreaction efficiency [23,24]. In order to improve the solar energy utilization rate and charge separation efficiency, a method of doping metallic and/or non-metallic elements, coupling with other semiconductors, and sensitizing the surface of the metal complex can be employed [25,26]. However, the doping of metal elements has poor thermal stability and high cost. In recent years, non-metallic elements have been increasingly used as doping elements in research. Because the atomic radius is close to O elements, such as N, C, F and B are often selected as non-metallic doping elements. During the process, part of O atoms is replaced by N atoms, which is beneficial to form the structural defects. Yu et al. [27] found that the doping of N significantly improves the light absorption of semiconductor catalysts such as ZnO. Since the p-orbital of the nitrogen atom and the 2p-orbital of the oxygen atom are similar and easy to hybridize [28], the doping of N can narrow the band-gap of the catalyst and generate partial OV defects, thereby expanding the range of response to visible light absorption.

In this work, based on the ZnCo-LDHs (layered double hydroxides), the N-ZnO/ZnCo₂O₄ composites were prepared via the hydrothermal method. After a series of characterization, the composition, morphology, chemical structure and optical properties of the synthesized samples were further investigated. In addition, the methylene blue (MB), methyl orange (MO) and rhodamine B (RhB) dyes were selected as the probe molecules to explore the photodegradation performance of the N-ZnO/ZnCo₂O₄ composites. Finally, the possible mechanism of photodegradation of the above dyes was discussed.

2. Experimental

2.1. Materials

During this work, all chemicals were the analytical grade without any further purification. Thiourea and Zn(NO₃)₂·6H₂O were both obtained from Xilong Chemical

Co., Ltd., (China). Co(NO₃)₂·6H₂O was purchased from Sinopharm Chemical Reagent Co., Ltd., (China). Urea and MO were obtained from Tianjin Hengxing Chemical Reagent Manufacturing Co., Ltd., (China). Ethylene glycol was received from Shanghai Titan Scientific Co., Ltd., (China). MB was supplied by Tianjin Chemical Reagent Research Institute Co., Ltd., (China) and RhB was obtained from Tianjin Kemiou Chemical Reagent Co., Ltd., (China). Deionized water was used throughout the experiment.

2.2. Synthesis of ZnCo-LDHs

The ZnCo-LDHs were prepared by the hydrothermal method, as schematically located in Fig. 1. Briefly, solution A containing Zn(NO₃)₂·6H₂O and Co(NO₃)₂·6H₂O (the initial Zn/Co molar ratio was equal to 2.5) was made in distilled water. Then, the urea was dissolved in an ethylene glycol-water mixture (V_{EG}/V_W was equal to 1), obtaining the mixed solution B. After the above two solutions were transferred to the Teflon-lined autoclave and heated at 150°C for 12 h. The obtained solid products were separated by centrifugation, then washing with distilled water and anhydrous ethanol several times. The resulting samples were dried overnight in an oven at 60°C.

2.3. Synthesis of N-ZnO/ZnCo₂O₄ composites

As a nitrogen source, the thiourea was mixed with the ZnCo-LDHs, then calcined at 500°C for 4 h in a tube furnace to obtain the N-ZnO/ZnCo₂O₄ composites. The ratios of nitrogen source and ZnCo-LDHs were 0, 1:1, 2:1, 3:1 and 3:2, respectively. The obtained photocatalysts were marked as ZC, RZC, NZC-1:1, NZC-2:1, NZC-3:1 and NZC-3:2, respectively.

2.4. Photocatalysts characterization

A powder X-ray diffractometer (XRD, D8 Advanced Bruker Co., Germany) was conducted to investigate the crystallinity and phase analysis of the photocatalysts. The specific surface morphology of the photocatalysts was measured by scanning electron microscopy (SEM, TESCAN MIRA3 LMU) and high-resolution transmission electron microscopy (HRTEM; Tecnai G² F20 S-Twin, FEI). X-ray photoelectron spectroscopy (XPS) analysis was recorded the chemical states of the elements using the ULVAC-PHI spectrometer at 3.0×10^{-10} mbar using Al K α X-ray beam (1,486.6 eV). The UV-vis diffuse reflectance spectroscopy was provided by spectrophotometer (Shimadzu 2401 spectrophotometer). The Fourier-transform infrared (FT-IR) spectra of composites embedded in KBr pellets were shown on an AVATAR 360 spectrometer (Nicolet Instrument Corporation, America). The Brunauer–Emmett–Teller and surface areas and pore size distribution of composites were recorded by nitrogen adsorption isotherms under the following conditions: 77 K, 8 h outgas, and 100°C in advance treatment.

2.5. Photocatalytic degradation activity test

The photocatalytic activities of catalysts were tested by degrading MB, MO and RhB using a 500 W

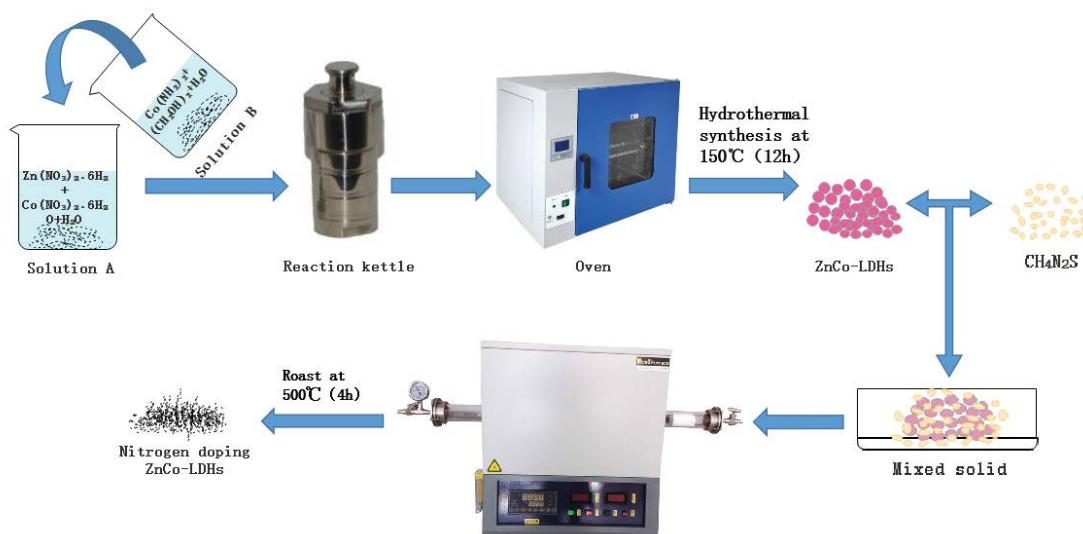


Fig. 1. Schematic representation of N-ZnO/ZnCo₂O₄.

high-pressure mercury lamp of a 400 nm optical cutoff filter. The as-prepared photocatalysts (0.05 g) were added to the MB solution (50 mL, 10 mg/L). Then, in order to achieve an adsorption–desorption equilibrium, the suspension solution was placed on a magnetic stirrer for 30 min under dark conditions. The solutions were then subjected to photocatalytic degradation which was exposed to the light irradiation, and this process should always be at room temperature. The equal of suspension solutions was sampled every 30 min, and the photocatalyst particles were removed by the filter. The absorbance of the solutions was measured at a wavelength of 664 nm by utilizing a UV-vis spectrophotometer (UV-9600) to analyze the concentration of MB. The catalyst with the optimal photocatalytic activity was evaluated by the above experimental procedure. The photocatalyst with the optimal photocatalytic activities was then used to photodegrade MO and RhB by the same method.

3. Results and discussion

3.1. Characterization of the catalyst

3.1.1. X-ray diffraction

Fig. 2 shows the X-ray diffraction (XRD) diffractions of N-ZnO/ZnCo₂O₄ composites with different doping ratio of N atom. The ZC exhibits reflection peaks around 25°, 32°, 37°, 43°, 47°, 54° and 62° corresponding to (006), (012), (015), (018), (101), (110) and (113) basal reflections, respectively, which are the typical features of the LDHs [29]. The XRD pattern of RZC shows that the characteristic peaks of ZC disappear at a calcination temperature of 500°C, indicating that the layered structure was destroyed. The characteristic peaks corresponding to ZnO and ZnCo₂O₄ appear, and the crystal faces (422), (440) and (400) belong to the ZnO phase (JCPDS no. 36-1451) and ZnCo₂O₄ phase (JCPDS #23-1390) [30–32]. After N doping, new peaks appear due to the overlap of peaks of ZnO/ZnCo₂O₄ and nitrogen

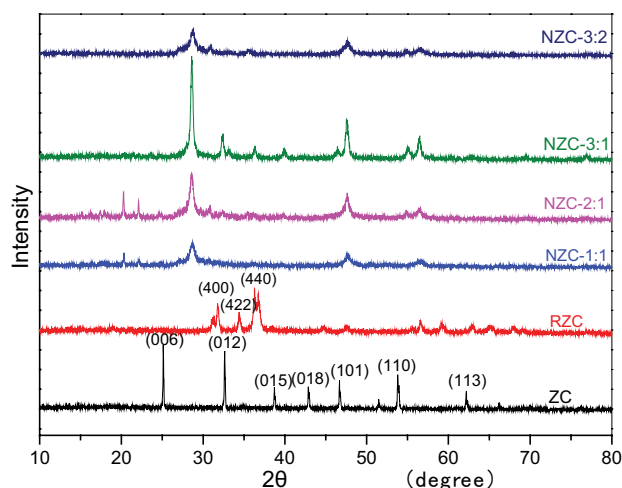


Fig. 2. XRD patterns of ZC, RZC, NZC-1:1, NZC-2:1, NZC-3:1 and NZC-3:2.

atoms. A strong peak is located around 29°, corresponding to the characteristic diffraction peak of ZnO. Therefore, it can be concluded that the introduction of nitrogen did not change the structure of ZnO.

3.1.2. Scanning electron microscopy

SEM images of the ZC, RZC and NZC-3:2 composites are shown in Fig. 3. As can be seen from Fig. 3a that ZC has a regular polyhedron shape and a distinct layered structure. The above features are the typical features of LDHs, indicating that the ZC precursors are successfully prepared by hydrothermal method. It can be seen from the SEM image of RZC (Fig. 3b) that after being calcined at 500°C, the RZC still maintains a distinct layered structure, and cracks appear on the surface of the material.

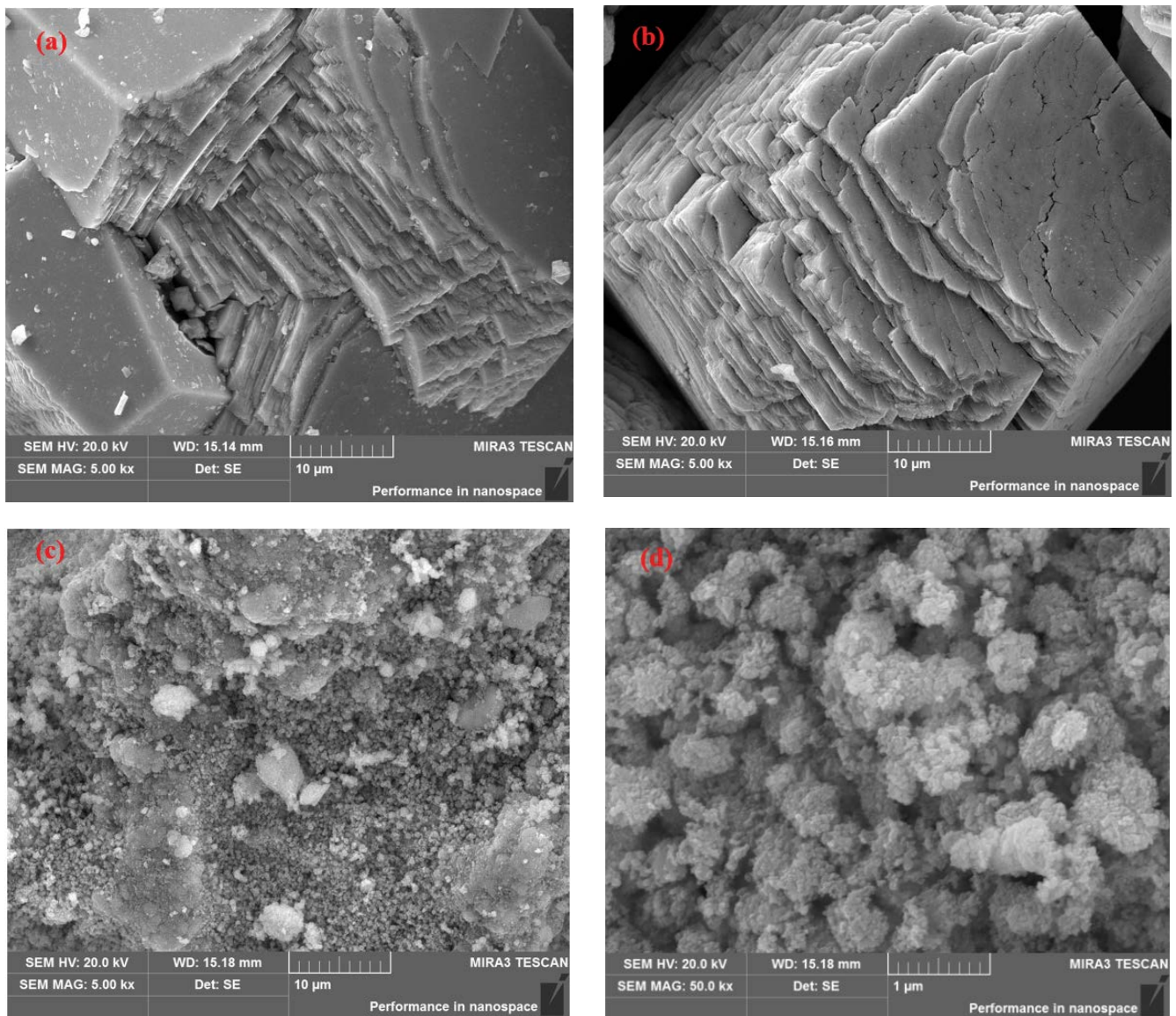


Fig. 3. SEM images of (a) ZC (10 μm), (b) RZC (10 μm), (c) NZC-3:2 (10 μm), and (d) NZC-3:2 (1 μm).

As shown in Fig. 3c and d, after the doping with N, the layered structure of NZC-3:2 collapsed and the sample showed a pelleted morphology with a fluffed structure.

3.1.3. Transmission electron microscopy

The morphology and structure of the NZC-3:2 composites were confirmed by transmission electron microscopy (TEM) and high-resolution TEM. TEM images of the as-prepared samples is shown in Fig. 4a, where the NZC-3:2 was formed by stacking many nanosheets, and each nanosheet was different in shape and size. It can be known from Fig. 4b that each nanosheet was composed of numerous small nanoparticles. Fig. 4c shows the HRTEM images of the NZC-3:2 composite, which clearly reveals two lattice plane separations of 0.2792 nm and 0.4625 nm, corresponding to the (101) plane of N-ZnO and the (111) plane of

ZnCo₂O₄. Energy-dispersive X-ray analysis of NZC-3:2 confirms that the composite is composed of Zn, Co, N, O and C, showing a good correlation with the obtained XRD and XPS results.

3.1.4. Fourier-transform infrared spectroscopy

Fig. 5 shows the FT-IR spectra of ZC, RZC and NZC-3:2. It shows that the broad absorption band with a high wave near 3,439 cm⁻¹ of ZC is attributed to the OH stretching vibration. The adsorption at 1,642 cm⁻¹ of ZC is derived from the O–H bending vibration of hydroxyl groups or interlayer water [33]. As for RZC and NZC-3:2, the peaks in the region from 400 to 560 cm⁻¹ are ascribed to the bending vibration Zn–O band [9,28]. The broad absorption band of NZC-3:2 at high wave number around 3,400 cm⁻¹ is due to the stretching vibration of N–H bonds [34].

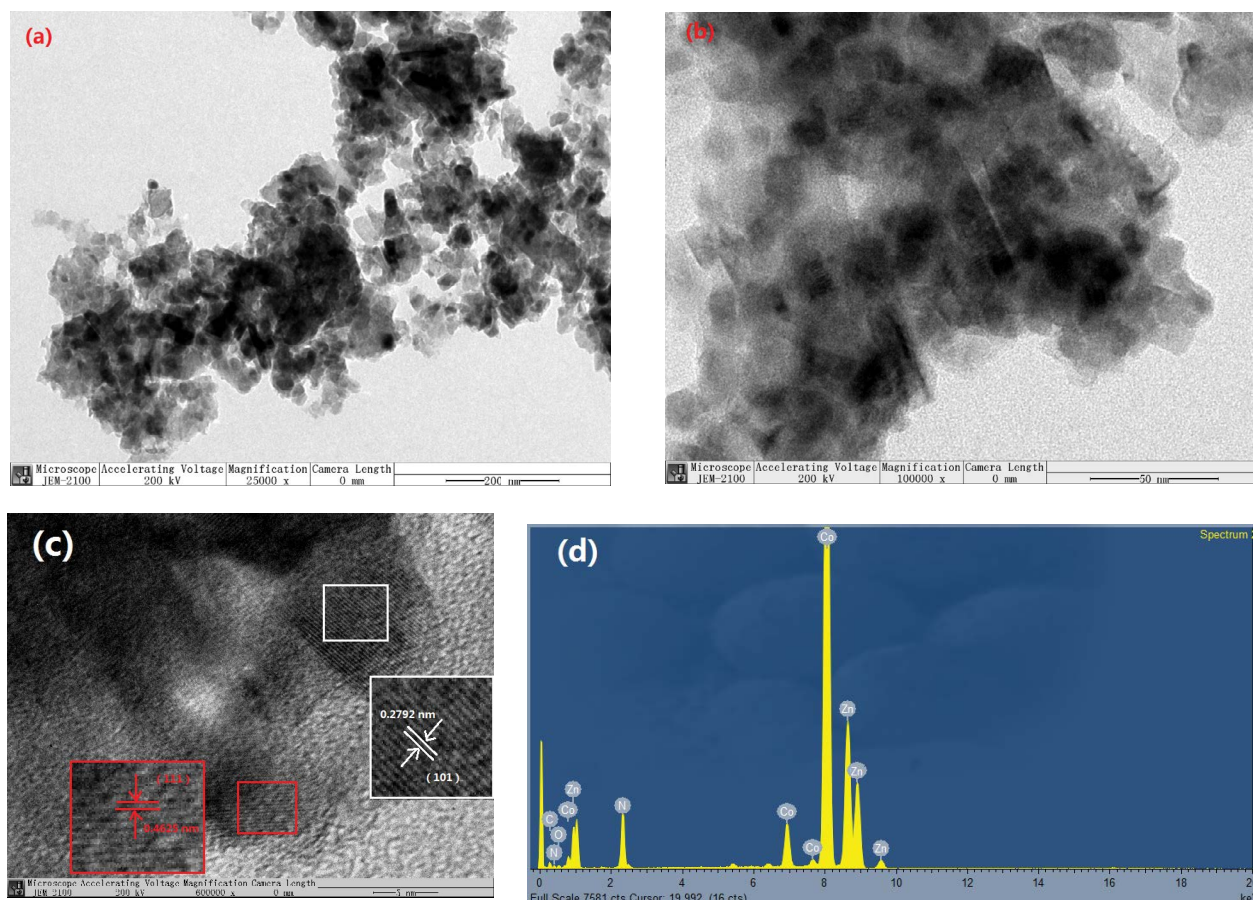


Fig. 4. TEM images of (a and b) NZC-3:2, HRTEM images of (c) NZC-3:2, and EDX spectrum of NZC-3:2.

3.1.5. X-ray photoelectron spectroscopy

The surface chemical composition of the prepared NZC-3:2 composites is analyzed by XPS. As shown in Fig. 6a, there are Zn, Co, O, N, and C elements in NZC-3:2. High-resolution XPS spectra of Zn 2p, Co 2p, O 1s and N 1s are shown in Figs. 6b–e. Two peaks are located at 1,023.1 and 1,046.7 eV in Fig. 6b corresponding to the levels of Zn 2p_{3/2} and Zn 2p_{1/2}, respectively. As shown in Fig. 6c, the two main peaks of the bond energy of the Co 2p orbital of 782.23 and 798.24 eV are attributed to Co 2p_{3/2} and Co 2p_{1/2}, respectively. The O 1s peak was subjected to nonlinear least-squares fitting to obtain two fitted peaks at 530.73 and 532.50 eV, respectively. The peak of 530.73 eV can be assigned to the O²⁻ ion in oxidation products. Another peak of 532.50 eV is ascribed to the chemical absorption of oxygen and/or hydroxyl on the surface of the photocatalyst [35]. It can be seen from the N 1s orbital spectrum of Fig. 5e that three different peak bond energies are 399.2, 398.8 and 397.4 eV, indicating that the N atom has been incorporated into the metal oxide lattice produced by the calcination of ZnCo-LDHs. Among them, the peak of 399.2 eV can be attributed to the O–N–Co bond, and that of 397.4 eV indicates that the N atom combines with the O vacancy on the surface of the crystal lattice to form an N–O–Zn or Zn–N–O bond [36]. The peak of 398.8 eV is due to the presence of an anion N in sp² hybrid N [37].

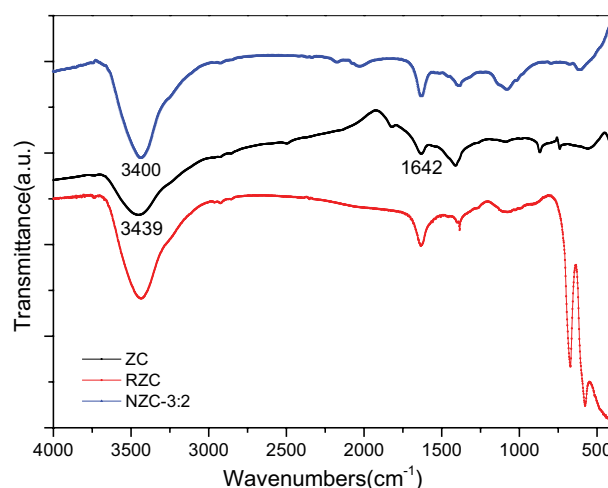


Fig. 5. FT-IR spectra of ZC, RZC, NZC-3:2.

3.1.6. N₂ adsorption–desorption experiments

The specific surface area and pore structure of the catalyst are investigated by N₂ adsorption–desorption experiments. Detailed pore structure parameters are shown in Table 1 and Fig. 7. We can see that the N₂ adsorption–desorption curves of ZC and NZC-3:2 belong to the type

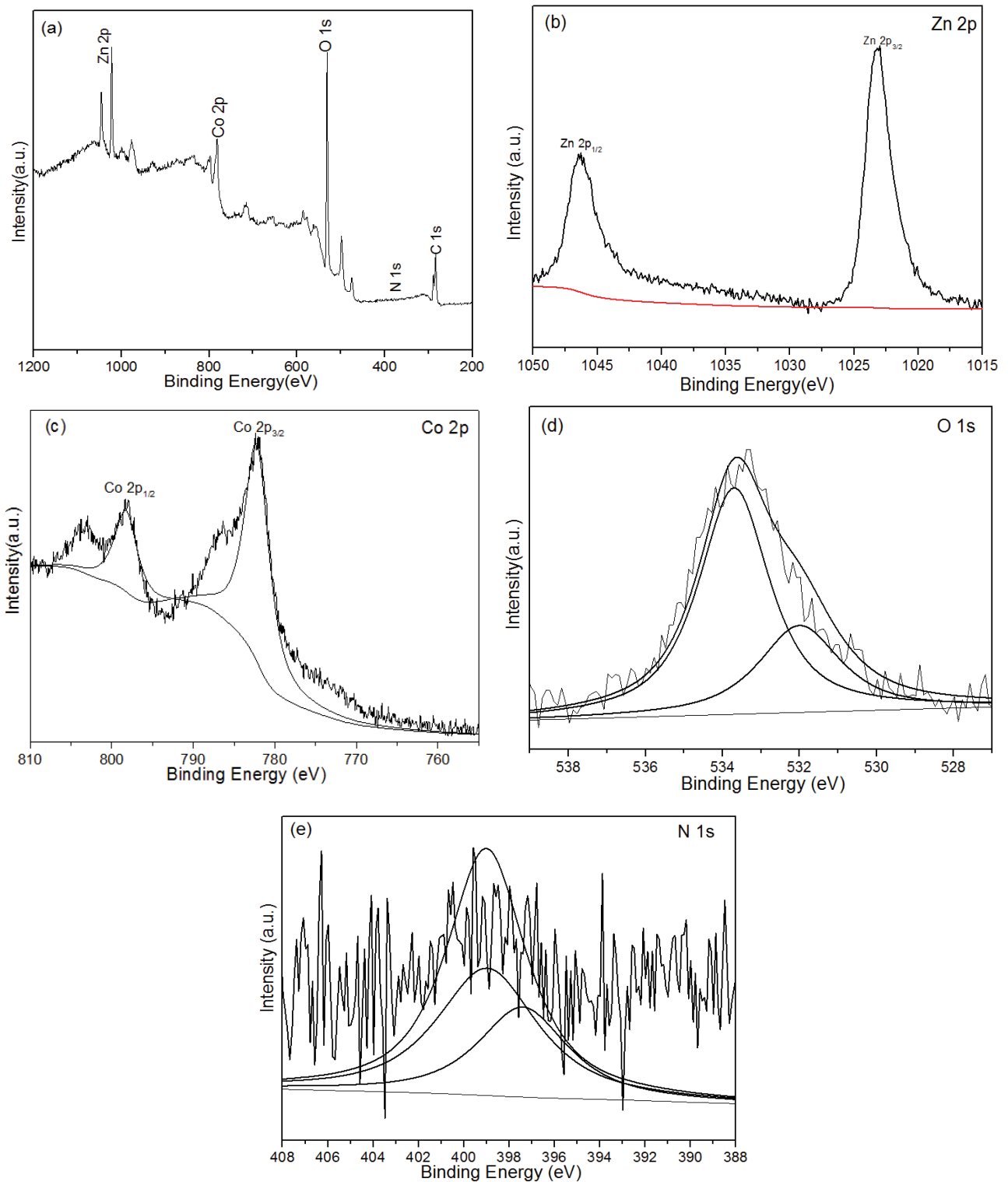


Fig. 6. XPS spectra of (a) NZC-3:2, (b) Zn 2p, (c) Co 2p, (d) O 1s, and (e) N 1s

IV with H4 hysteresis loop, indicating that the catalyst has a mesoporous structure. This result is consistent with the topographical features reflected by the SEM spectrum. Fig. 7b shows the pore size distribution curve of

the photocatalyst. It can be seen that the pore size range is substantially in the range of mesopores (2–50 nm), so that it has a relatively uniform mesoporous structure. As can be seen from Table 1, the specific surface area

Table 1
Physicochemical properties of the materials

Photocatalyst	Pore diameter (nm)	Pore volume (m ³)	Surface area (m ² /g)
ZC	1.943	0.142	40.527
NZC-3:2	2.197	0.205	62.340

and pore volume of the ZC precursor NZC-3:2 composite increased to 62.340 m²/g, which is advantageous for the improvement of catalytic activity. At the same time, the Barrett–Joyner–Halenda pore volume distribution is 0.205 m³, and the average pore diameter is about 2.197 nm. The above structure promotes the capture of dye molecules and the improvement of adsorption capacity.

3.1.7. UV-vis diffuse reflectance spectroscopy

The optical absorption properties of the ZC, RZC and NZC-3:2 composites were measured, and the results are shown in Fig. 8. The absorption edge of the ZC is about 390 nm, indicating that the absorption capacity of ZC is poor in the visible light band. After high-temperature calcination, the RZC has a clear absorption edge around 460 nm, proving that the ZnO and ZnCo₂O₄ phases enhance the response of RZC to the visible region. Compared with RZC, the NZC-3:2 composite presented a red-shift of the absorption edge to a higher wavelength, indicating that the doping of N atom enhanced the visible light adsorption [28]. At the same time, the bandgap energy of the electronic transition is reduced from 3.06 to 2.92 eV, indicating that the energy required for the electronic transition is reduced. The above result is attributed to the local point of the edge of the valence band induced by the N atom between the gaps, and synergy

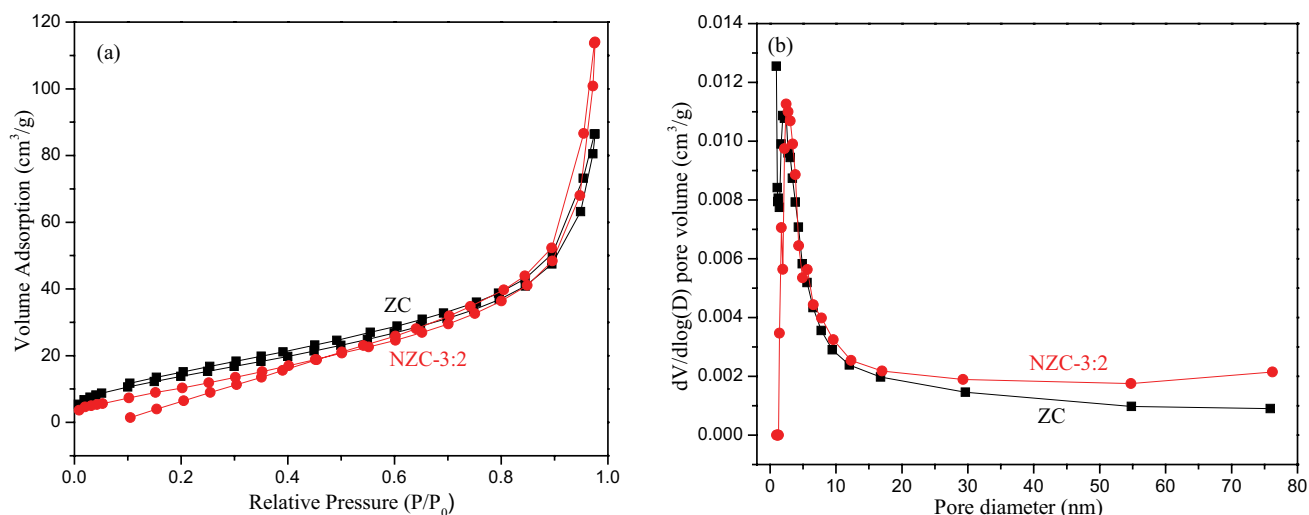


Fig. 7. (a) N₂ adsorption-desorption isotherms of ZC and NZC-3:2, (b) pore size distribution curves of ZC and NZC-3:2.

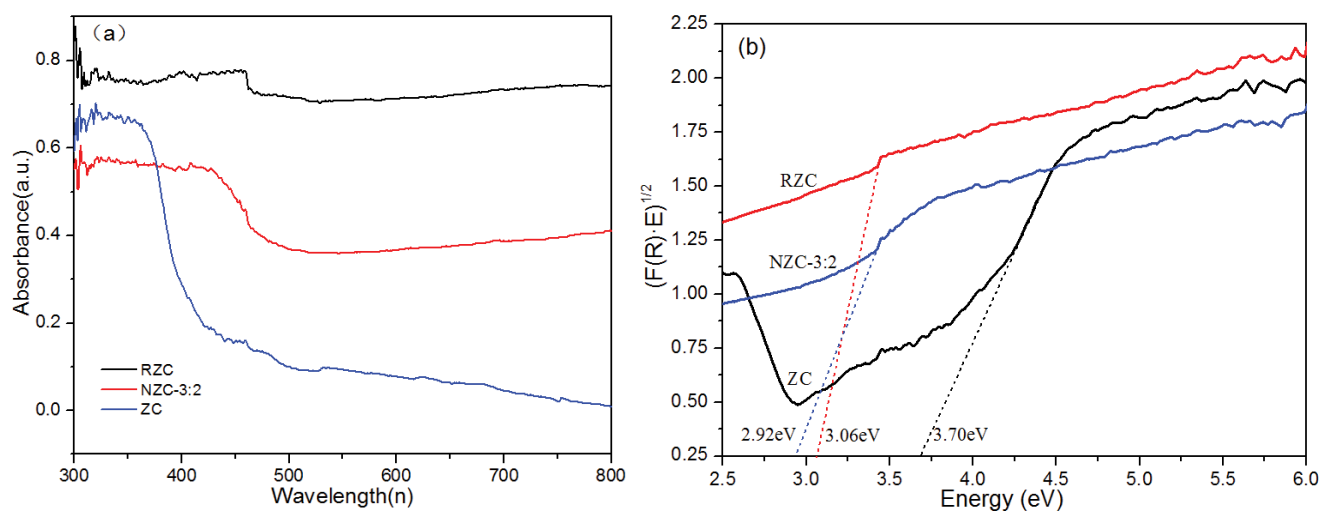


Fig. 8. (a) UV-vis diffuse reflectance spectra of ZC, RZC and NZC-3:2, (b) energy band gaps of ZC, RZC and NZC-3:2 composites.

with the oxygen vacancy acts to form a new energy band between the original valence band and the conduction band.

3.2. Photocatalytic activities of the catalysts

The photocatalytic activities of different photocatalysts were evaluated by the degradation of MB (50 mL,

10 mg/L) under visible light irradiation, as shown in Fig. 9. The adsorption capacities of MB on catalysts were investigated in darkroom conditions and demonstrated that the suspensions reach the adsorption–desorption equilibrium. In Fig. 9a, it is clearly seen that NZC-3:2 composites present the highest activity of photodegradation, and nearly 91.66% of MB was removed within 210 min. About

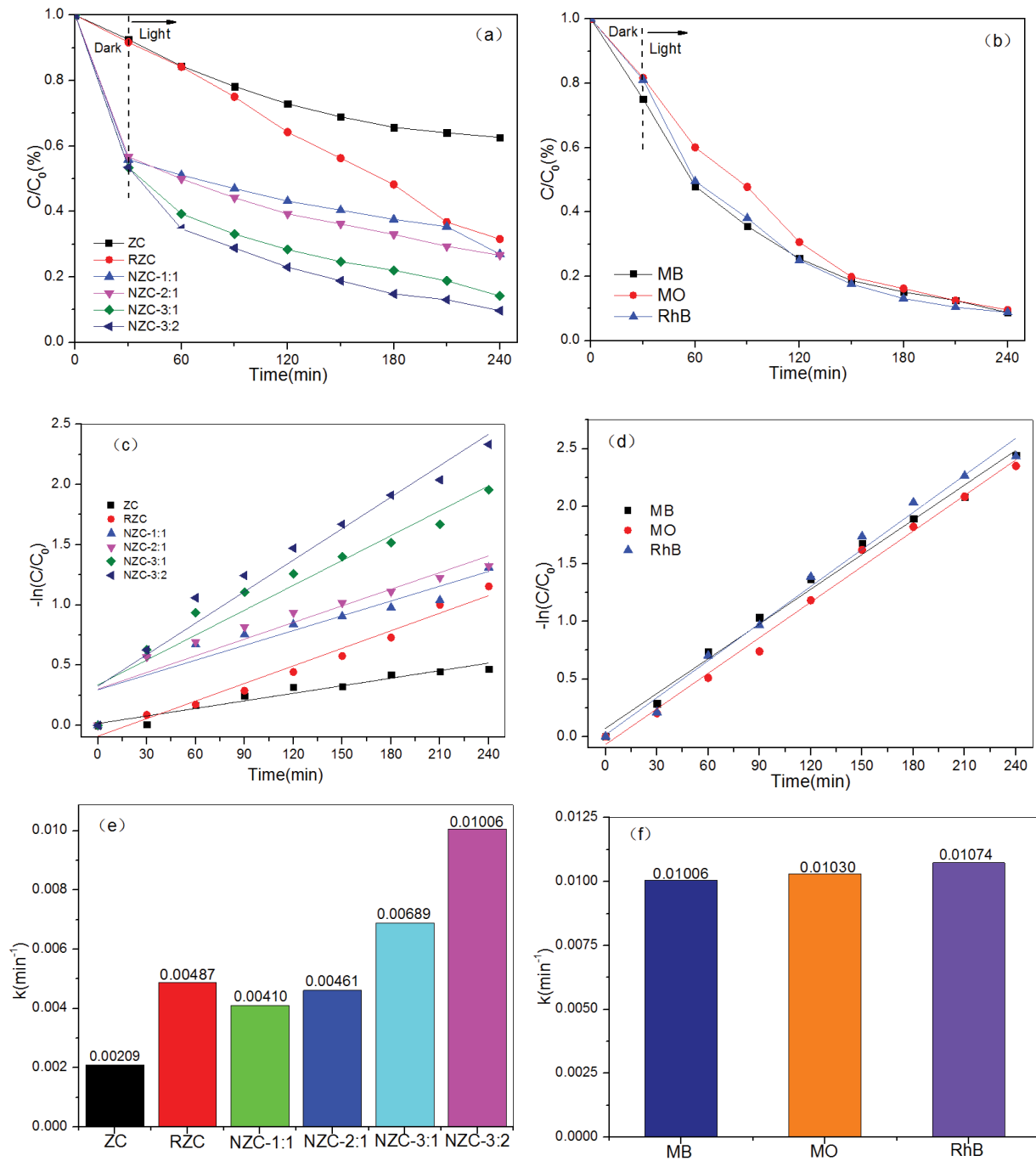


Fig. 9. (a) MB concentration as a function of time in different photocatalytic treatments, (b) MB, MO and RhB concentration as a function of time in NZC-3:2 treatments, (c) pseudo-first-order degradation kinetics for MB with different photocatalysts, used to estimate Langmuir–Hinshelwood coefficient, (d) pseudo-first-order degradation kinetics for MB, MO and RhB with NZC-3:2, (e) the rate constant k of MB with different photocatalysts, and (f) the rate constant k of MB, MO and RhB with NZC-3:2.

37.38% of the MB was degraded by ZC under the same condition.

In order to further verify the favorable activity of NZC-3:2 hybrid composites, the NZC-3:2 composite was selected for photodegradation of MO (50 mL, 10 mg/L) and RhB (50 mL, 10 mg/L) under the same conditions. The result is shown in Fig. 9b, 90.95% of the MO and 91.22% of the RhB were degraded by NZC-3:2, demonstrating the good performance of NZC-3:2 in photodegradation. Since the introduction of N atom has an inhibitory effect on the recombination of photogenerated charge carriers, the photocatalytic activity of NZC is improved. The NZC composites exhibited good photocatalytic activity, because the doping of N atoms changes the original electron band structure and increases the oxygen vacancies in the gap, thus absorbing more photons under illumination conditions [38].

The kinetic behavior of photocatalytic degradation was analyzed, and the experimental data were consistent with the Langmuir–Hinshelwood model. The photocatalytic process of dyes followed the pseudo-first-order kinetics, which could be described by the following equation: $-\ln(C/C_0) = k_a t$, where k_a stands for the apparent pseudo-first-order rate constant (min^{-1}), C_0 represents the initial concentration of the dyes (mg/L), and C is the concentration of the dyes (mg/L) of the reaction time. Figs. 9c and d show the corresponding relationship of $\ln(C_0/C)$ to the photodegradation irradiation time of the target dyes, and the linear relationship confirms that the photodegradation experiment follows the pseudo-first-order kinetics [39]. The calculated first-order rate constants are shown in Figs. 9d and e, respectively. The reaction rate constant of NZC-3:2 (0.01006 min^{-1}) is about 4.8 times compared with that of ZC (0.00209 min^{-1}). Fig. 9f further demonstrates that the NZC-3:2 composites have similar kinetic constants for the degradation of MO and RhB, respectively. According to the results, we can infer that it could greatly improve the photocatalytic efficiency of the NZC-3:2 composite by doping N into RZC.

3.3. Photocatalytic stability of catalysts

Considering the importance of photocatalyst stability in practical applications, five sets of cycle experiments were performed to test the stability of catalysts. After completing every degradation reaction of the samples, the powder of composite was collected by filtration. The collected powder was then added to the fresh target dye of the same initial concentration for the next photocatalysis. As found in Fig. 10, the photocatalytic activity of the NZC-3:2 composites still maintains about 75% of its initial activity after being recycled five times, demonstrating that the samples have remarkable stability and reusability for potential practical applications in environmental purification.

3.4. Photocatalytic mechanism of catalysts

In this work, the mixed metal oxides were obtained including ZnO and ZnCo_2O_4 phases after calcining the ZnCo-LDHs. Because the N atoms enter into the lattice of oxidation products, the original electronic bandstructure was changed, and the oxygen vacancies in the gap were increased. Thus, the N-ZnO/ ZnCo_2O_4 composites can absorb

more photons from light irradiation conditions and narrow the band gap from 3.7 to 2.92 eV, which greatly reduce the required energy for electronic transitions and improve the utilization of visible light.

Fig. 11 shows the possible mechanism of the N-ZnO/ ZnCo_2O_4 composites for dye degradation. Under visible light irradiation, the formed electron-hole pair results in excited state electrons to be transported from valence band (VB) to conduction band (CB). The quasi-continuous energy levels are formed when the oxygen defects are located at the interface of N-ZnO/ ZnCo_2O_4 , which induces the formation of ohmic contact and lower the interfacial electric resistance. The holes in the VB is recombined with photo-induced electrons at the CB through the ohmic contact. As a result, the electrons and holes in the CB and the VB are isolated commendably. Therefore, photogenerated electrons in samples are available to photodegrade the dyes. At the same time, oxygen molecules are reduced by the greater negative potential of the photo-induced electrons, which in turn produces superoxide anions ($\text{O}_2^{\cdot-}$) results in the degradation of the contaminants. The holes at VB of NZC-3:2 are photo-excited to directly oxidize the dye, and the obtained intermediate reacts with H_2O to form hydroxyl radicals (OH^{\cdot}), both of which are the main active substances in the photocatalytic reaction [40,41]. Thus, we present that the N-ZnO/ ZnCo_2O_4 composites can enhance the separation of electron-hole pairs and reduce the recombination of charge carriers, resulting in an increase in the photodegradation process.

4. Conclusion

In summary, we developed a hydrothermal method to prepare the N-ZnO/ ZnCo_2O_4 composites. The characteristics of the as-prepared catalysts were systematically detected, indicating that the NZC-3:2 composites have the optimal ability of visible-light harvesting and can effectively separate photogenerated charges. The NZC-3:2 composites showed higher efficiency of photodegradation than that of ZC for the degradation of MB, MO and RhB. Moreover, NZC-3:2 composites had good stability after five cycle runs.

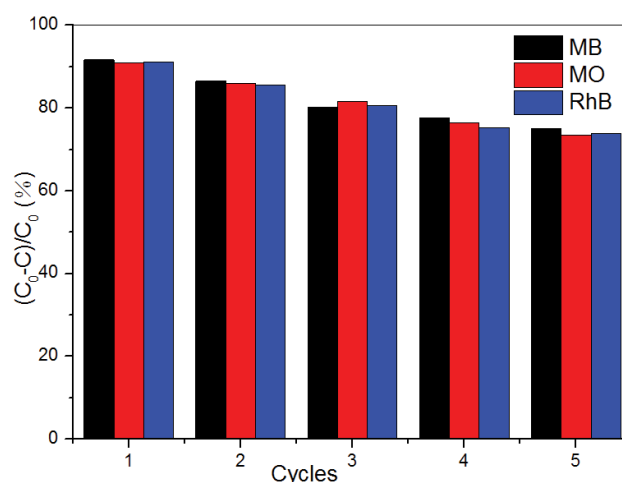


Fig. 10. Photocatalytic cycles of NZC-3:2 hybrid composites at pH 7.0 under visible light irradiation.

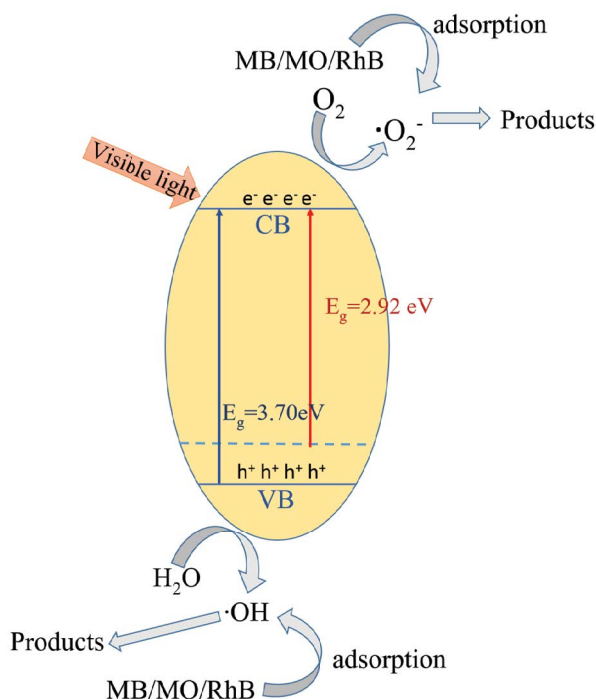


Fig. 11. Proposed photocatalytic mechanism of NZC-3:2 hybrid composites for dye solution degradation.

Finally, the possible degradation mechanism of dyes was proposed.

Acknowledgements

This financial supports from the National Natural Science Foundation of China (No. 21776319), the Hunan Provincial Science and Technology Plan Project, China (No. 2018TP1003) and the Fundamental Research Funds for the Central Universities of Central South University (No.2019zzts444).

References

- [1] D.Z. Lu, M.C. Yang, K.K. Kumar, P. Wu, D. Neena, Investigation of structure and photocatalytic degradation of organic pollutants for protonated anatase/titanate nanosheets during thermal treatment, *ACS Sustainable Chem. Eng.*, 6 (2018) 4801–4808.
- [2] S. Anandan, V.K. Ponnusamy, M. Ashokkumar, A review on hybrid techniques for the degradation of organic pollutants in aqueous environment, *J. Ultrason. Sonochem.*, 67 (2020) 105130, <https://doi.org/10.1016/j.ultsonch.2020.105130>.
- [3] M. Faraz, F.K. Naqvi, M. Shakir, N. Khare, Synthesis of samarium-doped zinc oxide nanoparticles with improved photocatalytic performance and recyclability under visible light irradiation, *New J. Chem.*, 42 (2018) 2295–2305.
- [4] H. Kotani, T. Suenobu, Y.-M. Lee, W.W. Nam, S. Fukuzumi, Photocatalytic generation of a non-heme oxoiron(IV) complex with water as an oxygen source, *J. Am. Chem. Soc.*, 133 (2011) 3249–3251.
- [5] T. Ochiai, A. Fujishima, Photoelectrochemical properties of TiO_2 photocatalyst and its applications for environmental purification, *J. Photochem. Photobiol., C*, 13 (2012) 247–262.
- [6] Z. Ming, W.S. Zhu, H.P. Li, S.H. Xun, M. Li, Y.N. Li, Y.C. Wei, H.M. Li, Fabrication and characterization of tungsten-containing mesoporous silica for heterogeneous oxidative desulfurization, *Chin. J. Catal.*, 37 (2016) 971–978.
- [7] Y. Zhou, Z.Y. Zhao, F. Wang, K. Cao, D.E. Doronkin, F. Dong, J.-D. Grunwaldt, Facile synthesis of surface N-doped $\text{Bi}_2\text{O}_3\text{CO}_3$: origin of visible light photocatalytic activity and in situ DRIFTS studies, *J. Hazard. Mater.*, 307 (2016) 163–172.
- [8] M. Pirhashemi, A. Habibi-Yangjeh, S.R. Pouran, Review on the criteria anticipated for the fabrication of highly efficient ZnO-based visible-light-driven photocatalysts, *J. Ind. Eng. Chem.*, 62 (2018) 1–25.
- [9] M. Shekofteh-Gohari, A. Habibi-Yangjeh, A. Masoud, R. Afsar, Magnetically separable nanocomposites based on ZnO and their applications in photocatalytic processes: a review, *Crit. Rev. Env. Sci. Technol.*, 48 (2018) 806–857.
- [10] P.W. Huo, M.J. Zhou, Y.F. Tang, X.L. Liu, C.C. Ma, L.B. Yu, Y.S. Yan, Incorporation of N-ZnO/CdS/Graphene oxide composite photocatalyst for enhanced photocatalytic activity under visible light, *J. Alloys Compd.*, 670 (2016) 198–209.
- [11] Z. Somayeh, A. Habibi-Yangjeh, M. Mitra, BiOBr and AgBr co-modified ZnO photocatalyst: a novel nanocomposite with p-n-n heterojunctions for highly effective photocatalytic removal of organic contaminants, *J. Photochem. Photobiol., A*, 379 (2019) 11–23.
- [12] S.L. Cao, S. Shrestha, J.R. Li, X.B. Yu, J.Y. Chen, F. Yan, G.Y. Ying, C. Gu, L. Wang, G. Chen, Melatonin-mediated mitophagy protects against early brain injury after subarachnoid hemorrhage through inhibition of NLRP3 inflammasome activation, *Sci. Rep.*, 7 (2017) 2417, doi: 10.1038/s41598-017-02679-z.
- [13] J.Q. Wen, X. Li, W. Liu, Y.P. Fang, J. Xie, Y.H. Xu, Photocatalysis fundamentals and surface modification of TiO_2 nanomaterials, *Chin. J. Catal.*, 36 (2015) 2049–2070.
- [14] Z. Somayeh, A. Habibi-Yangjeh, M. Mitra, Fabrication of novel ZnO/BiOBr/C-Dots nanocomposites with considerable photocatalytic performances in removal of organic pollutants under visible light, *Adv. Powder Technol.*, 30 (2019) 1197–1209.
- [15] F.C. Lei, Y.F. Sun, K.T. Liu, S. Gao, L. Liang, B.C. Pan, Y. Xie, Oxygen vacancies confined in ultrathin indium oxide porous sheets for promoted visible-light water splitting, *J. Am. Chem. Soc.*, 136 (2014) 6826–6829.
- [16] B. Chica, C.-H. Wu, Y.G. Liu, M.W.W. Adams, T.Q. Lian, R.B. Dyer, Balancing electron transfer rate and driving force for efficient photocatalytic hydrogen production in CdSe/CdS nanorod-[NiFe] hydrogenase assemblies, *Energy Environ. Sci.*, 10 (2017) 2245–2255.
- [17] J.Q. Yan, T. Wang, G.J. Wu, W.L. Dai, N.J. Guan, L.D. Li, J.L. Gong, Tungsten oxide single crystal nanosheets for enhanced multichannel solar light harvesting, *Adv. Mater.*, 27 (2015) 1580–1586.
- [18] A. Naldoni, M. Allietta, S. Santangelo, M. Marelli, F. Fabbri, S. Cappelli, C.L. Bianchi, R. Psaro, V. Dal Santo, Effect of nature and location of defects on bandgap narrowing in black TiO_2 nanoparticles, *J. Am. Chem. Soc.*, 134 (2012) 7600–7603.
- [19] Y.H. Lv, W.Q. Yao, R.L. Zong, Y.F. Zhu, Fabrication of wide-range-visible photocatalyst Bi_2WO_6 nanoplates via surface oxygen vacancies, *Sci. Rep.*, 6 (2016) 19347.
- [20] H. Hirakawa, M. Hashimoto, Y. Shiraiishi, T. Hirai, Selective nitrate-to-ammonia transformation on surface defects of titanium dioxide photocatalysts, *ACS Catal.*, 7 (2017) 3713–3720.
- [21] G.K. Panchamoorthy, N.V. Madhav, A. Krishnan, R. Malolan, G. Rangarajan, Present applications of titanium dioxide for the photocatalytic removal of pollutants from water: a review, *J. Environ. Manage.*, 270 (2020) 110–906.
- [22] H.Y. Zhu, R. Jiang, J.B. Li, Y.Q. Fu, S.T. Jiang, J. Yao, Magnetically recyclable $\text{Fe}_3\text{O}_4/\text{Bi}_2\text{S}_3$ microspheres for effective removal of Congo red dye by simultaneous adsorption and photocatalytic regeneration, *Sep. Purif. Technol.*, 179 (2017) 184–193.
- [23] N. Serpone, Is the band gap of pristine TiO_2 narrowed by anion- and cation-doping of titanium dioxide in second-generation photocatalysts, *J. Phys. Chem. B*, 110 (2006) 24287–24293.
- [24] W. Cui, J.Y. Li, F. Dong, Y.J. Sun, G.M. Jiang, W.L. Cen, S.C. Lee, Z.B. Wu, Highly efficient performance and conversion pathway of photocatalytic NO oxidation on SrO-clusters@amorphous carbon nitride, *Environ. Sci. Technol.*, 38 (2017) 10746–10753.

- [25] M. Ahmad, E. Ahmed, Z.L. Hong, N.R. Khalid, W. Ahmed, A. Elhissi, Graphene–Ag/ZnO nanocomposites as high performance photocatalysts under visible light irradiation, *J. Alloys Compd.*, 577 (2013) 717–727.
- [26] G.Q. Zhao, D. Zhang, J.G. Yu, Y. Xie, W.J.H. Hu, F.P. Jiao, Multi-walled carbon nanotubes modified Bi₂S₃ microspheres for enhanced photocatalytic decomposition efficiency, *Ceram. Int.*, 43 (2017) 15080–15088.
- [27] W.L. Yu, J.F. Zhang, T.Y. Peng, New insight into the enhanced photocatalytic activity of N-, C- and S-doped ZnO photocatalysts, *Appl. Catal., B*, 181 (2016) 220–227.
- [28] S. Kumar, A. Baruah, S. Tonda, B. Kumar, V. Shanker, B. Sreedhar, Cost-effective and eco-friendly synthesis of novel and stable N-doped ZnO/g-C₃N₄ core-shell nanoplates with excellent visible-light responsive photocatalysis, *Nanoscale*, 6 (2014) 4830–4842.
- [29] J.C. Sun, Y.B. Zhang, J. Cheng, H. Fan, J.Y. Zhu, X. Wang, S.Y. Ai, Synthesis of Ag/AgCl/Zn-Cr LDHs composite with enhanced visible-light photocatalytic performance, *J. Mol. Catal. A: Chem.*, 382 (2014) 146–153.
- [30] J.Z. Kong, H.F. Zhai, W. Zhang, Visible light-driven photocatalytic performance of N-doped ZnO/g-C₃N₄ nanocomposites, *Nanoscale Res. Lett.*, 12 (2017) 526.
- [31] Y.G. Shi, Y.L. Zhu, B. Yu, Z. Gui, S.K. She, R.K.K. Yuen, H. Liu, Y. Hu, Enhanced thermal stability of polystyrene by graphitic carbon nitride/spinel ZnCo₂O₄ nanohybrids and the catalytic mechanism investigation, *RSC Adv.*, 5 (2015) 41835–41838.
- [32] Z.H. Pu, Q. Liu, C. Tang, A.M. Asiri, A.H. Qusti, A.O. Al-Youbi, X.P. Sun, Spinel ZnCo₂O₄/N-doped carbon nanotube composite: a high active oxygen reduction reaction electrocatalyst, *J. Power Sources*, 257 (2014) 170–173.
- [33] X.C. Wang, K. Maeda, A. Thomas, K. Takanabe, G. Xin, J.M. Carlsson, K. Domen, M. Antonietti, A metal-free polymeric photocatalyst for hydrogen production from water under visible light, *Nat. Mater.*, 8 (2009) 76–80.
- [34] H.T. Lu, Z.L. Zhu, H. Zhang, J.Y. Zhu, Y.L. Qiu, Simultaneous removal of arsenate and antimonate in simulated and practical water samples by adsorption onto Zn/Fe layered double hydroxide, *Chem. Eng. J.*, 276 (2015) 365–375.
- [35] H.W. Bai, Z.Y. Liu, D.D. Sun, Hierarchical nitrogen-doped flowerlike ZnO nanostructure and its multifunctional environmental applications, *Chem.-Asian J.*, 7 (2012) 1772–1780.
- [36] X.Y. Yang, A. Wolcott, G.M. Wang, A. Sobo, R.C. Fitzmorris, F. Qian, J.Z. Zhang, Y. Li, Nitrogen-doped ZnO nanowire arrays for photoelectrochemical water splitting, *Nano Lett.*, 9 (2009) 2331–2336.
- [37] J.Z. Jiang, J. Zou, A.T.S. Wee, W.J. Zhang, Use of single-layer g-C₃N₄/Ag hybrids for surface-enhanced Raman scattering (SERS), *Sci. Rep.-UK*, 6 (2016) 34599–34510.
- [38] C.S. Zhu, J.T. Zheng, L.Y. Fang, P. Hu, Y.K. Liu, X.Q. Cao, M.B. Wu, Advanced visible-light driven photocatalyst with enhanced charge separation fabricated by facile deposition of Ag₃PO₄ nanoparticles on graphene-like h-BN nanosheets, *J. Mol. Catal. A: Chem.*, 424 (2016) 135–144.
- [39] X. Wu, D. Zhang, F.P. Jiao, S. Wang, Visible-light-driven photodegradation of methyl orange using Cu₂O/ZnAl calcined layered double hydroxides as photocatalysts, *Colloids Surf., A*, 508 (2016) 110–116.
- [40] S.-J. Xia, F.-X. Liu, Z.-M. Ni, J.-L. Xue, P.-P. Qian, Layered double hydroxides as efficient photocatalysts for visible-light degradation of Rhodamine B, *J. Colloid Interface Sci.*, 405 (2013) 195–200.
- [41] F. Cao, W.D. Shi, L.J. Zhao, S.Y. Song, J.H. Yang, Y.Q. Lei, H.J. Zhang, Hydrothermal synthesis and high photocatalytic activity of 3D Wurtzite ZnSe hierarchical nanostructures, *J. Phys. Chem. C*, 112 (2008) 17095–17101.

Supplementary information

The weight percentages of the elements in the NZC-3:2 are provided in Table S1. The EDX data shows the existence of Zn and Co, and the molar ratio of Zn/Co was approximately 2.5/1, which was in accordance with the composition of the precursor solution.

Table S1
Weight percentage of elements in the NZC-3:2

Element	Weight (%)	Atomic (%)
N	9.42	20.09
Zn	60.04	25.75
Co	24.18	32.62
O	6.35	21.54
Totals	100.00	